



Angular Sizes, Radii, and Effective Temperatures of B-type Stars from Optical Interferometry with the CHARA Array

Kathryn D. Gordon¹ , Douglas R. Gies¹ , Gail H. Schaefer² , Daniel Huber³ , and Michael Ireland⁴ 

¹ Center for High Angular Resolution Astronomy and Department of Physics and Astronomy, Georgia State University, P.O. Box 5060, Atlanta, GA 30302-5060, USA; kgordon@astro.gsu.edu

² The CHARA Array of Georgia State University, Mount Wilson Observatory, Mount Wilson, CA 91023, USA

³ Institute for Astronomy, University of Hawai'i, 2680 Woodlawn Drive, Honolulu, HI 96822, USA

⁴ Research School of Astronomy & Astrophysics, Australian National University, Canberra, ACT 2611, Australia

Received 2018 December 20; revised 2019 February 1; accepted 2019 February 2; published 2019 March 7

Abstract

We present interferometric observations of 25 spectral type-B stars that were made with the Precision Astronomical Visible Observations and the CLassic Interferometry with Multiple Baselines beam combiners at the Center for High Angular Resolution Astronomy Array (CHARA). The observations provide the angular sizes of these stars with an average error of 6%. The stars range in size from 1.09 mas for β Tau down to 0.20 mas for 32 Ori. We collected ultraviolet to infrared spectrophotometry and derived temperatures, angular diameters, and reddening estimates that best fit the spectra, as well as solutions with the angular size fixed by the interferometric measurements. There is generally good agreement between the observed and spectral fit angular diameters, indicating that the fluxes predicted from model atmospheres are reliable. On the other hand, the temperatures derived from angular diameters and fluxes tend to be larger (by $\approx 4\%$) than those from published results based on analysis of the line spectrum. This discrepancy may in part be attributed to unexplored atmospheric parameters or the existence of unknown companions. The physical radii of the stars are calculated from the angular diameters and *Gaia* DR2 parallaxes, and the target stars are placed in the Hertzsprung–Russell diagram for comparison with evolutionary tracks.

Key words: stars: early-type – stars: fundamental parameters – stars: massive – techniques: interferometric

Supporting material: figure sets, machine-readable tables

1. Introduction

Massive stars are rare but have a profound impact on their surroundings through their intense radiation and explosive deaths as supernovae, which seed the interstellar medium with the elements that make subsequent generations of stars and planets. Understanding their structure and evolution is based primarily on comparisons with stellar evolutionary tracks in the Hertzsprung–Russell (HR) diagram of temperature and luminosity, so determining these fundamental properties is a central focus of stellar astrophysics. The determination of an effective temperature T_{eff} for the hot and intermediate-mass B-type stars is generally accomplished by continuum flux measurements or by detailed analysis of the line spectrum, and both methods rely on comparisons with predictions from stellar model atmospheres. Fitzpatrick & Massa (1999, 2005) made fits of the ultraviolet and optical continuum spectra of a large sample of B stars using flux models from the ATLAS code to derive T_{eff} as well as gravity $\log g$, metallicity, microturbulent velocity, and interstellar reddening $E(B - V)$. These fits lead directly to estimates of the apparent limb-darkened angular diameter of the star θ_{LD} . Fitzpatrick & Massa (2005) combined the angular diameter with a distance from the *Hipparcos* parallax to then plot the stellar parameters in an HR diagram of $(\log T_{\text{eff}}, \log R/R_{\odot})$. The second method is based on an analysis of the line spectrum that yields the stellar temperature and gravity from measurements of the atomic ionization balance and the pressure broadening of the hydrogen lines (Nieva & Przybilla 2014; Mugnes & Robert 2015). This is an essential first step in chemical abundance analyses, and it leads to placement in another version of the HR diagram of

$(\log T_{\text{eff}}, \log g)$. Because of the critical role that atmospheric models play in our understanding of such massive stars, it is important to test them through independent means.

Here we use direct measurements of the stellar angular diameters to test atmospheric models and their flux predictions for the B-type stars, using the same methods as recently applied to a number of hot O-type stars (Gordon et al. 2018). The effective temperature is derived from the relationship between the extinction-corrected bolometric flux, angular diameter θ , and T_{eff} : $f_{\text{bol}} = \frac{1}{4}\theta^2\sigma T_{\text{eff}}^4$. This method was pioneered by Hanbury Brown et al. (1974), who measured 32 bright stars in the spectral range from O5 to F8 with the Narrabri Stellar Intensity Interferometer (NSII) to determine angular diameters. The physical radii follow once an accurate parallax and distance are available, and then the stars can be plotted in HR diagrams of $(\log T_{\text{eff}}, \log R/R_{\odot})$ or $(\log T_{\text{eff}}, \log L/L_{\odot})$.

This method is now seeing wide application thanks to observations made possible with long-baseline interferometry at the Center for High Angular Resolution Astronomy (CHARA) Array (ten Brummelaar et al. 2005) and elsewhere. Accurately measured angular diameters are combined with the stellar energy distributions (SEDs) to obtain effective temperature estimates for the relatively nearby stars. Maestro et al. (2013) presented a study of 10 early-type stars with spectral types from B2 to F6 that was based on observations with the Precision Astronomical Visible Observations (PAVO) beam combiner (Ireland et al. 2008) at the CHARA Array. They combined their measured angular diameters with SED fitting to estimate T_{eff} (two of their targets are included in our sample). Challouf et al. (2014) observed eight early-type stars ranging from spectral type B1 to A1 with the Visible spECTroGraph and

Table 1
Parameters of Sample Stars

ID	Star Name	HD Number	Spectral Class	V (mag)	$B - V$ (mag)	$V - K$ (mag)	T_{eff} (kK)	$\log g$ (c.g.s.)	$v \sin i$ (km s $^{-1}$)
1	λ Cas	2772	B8 Vn	4.73	-0.10	-0.13	11.9 \pm 0.6	4.00 \pm 0.25	220
2	ζ Cas	3360	B2 IV	3.66	-0.19	-0.59	21.5 \pm 0.5	3.91 \pm 0.03	17
3	γ Ari	11502	B9 V	4.83	-0.03	-0.09	10.0 \pm 1.0	4.50 \pm 0.25	142
4	73 Cet	15318	B9 III	4.28	-0.05	-0.09	10.6 \pm 1.0	4.00 \pm 0.25	57
5	17 Tau	23302	B6 III	3.70	-0.11	-0.22	14.7 \pm 1.0	3.03 \pm 0.25	152
6	20 Tau	23408	B8 III	3.87	-0.07	-0.12	13.8 \pm 1.0	3.50 \pm 0.25	37
7	27 Tau	23850	B8 III	3.63	-0.09	-0.16	13.0 \pm 1.0	3.50 \pm 0.25	182
8	τ Tau	29763	B3 V	4.28	-0.12	-0.36	16.6 \pm 1.0	4.00 \pm 0.25	147
9	β Tau	35497	B7 III	1.65	-0.13	-0.38	13.6 \pm 0.1	3.80 \pm 0.25	67
10	32 Ori	36267	B5 V	4.20	-0.13	-0.41	16.3 \pm 0.7	4.40 \pm 0.25	166
11	σ Leo	98664	B9.5V	4.05	-0.06	-0.10	10.5 \pm 0.1	3.90 \pm 0.25	60
12	η UMa	120315	B3 V	1.86	-0.19	-0.49	17.7 \pm 0.3	4.00 \pm 0.25	158
13	τ Her	147394	B5 IV	3.89	-0.15	-0.39	15.4 \pm 0.7	3.86 \pm 0.07	33
14	ζ Dra	155763	B6 III	3.17	-0.11	-0.31	13.5 \pm 0.8	3.99 \pm 0.17	40
15	ι Her	160762	B3 IV	3.80	-0.17	-0.43	18.2 \pm 1.0	3.82 \pm 0.13	10
16	γ Lyr	176437	B9 III	3.24	-0.05	0.05	10.4 \pm 0.6	3.50 \pm 0.25	65
17	λ Aql	177756	B9 Vn	3.44	-0.09	-0.22	10.7 \pm 1.0	4.15 \pm 0.05	125
18	ι Aql	184930	B5 III	4.36	-0.08	-0.12	13.9 \pm 0.5	3.64 \pm 0.25	65
19	δ Cyg	186882	B9.5 IV	2.87	-0.02	0.04	10.4 \pm 0.4	3.40 \pm 0.25	142
20	α Del	196867	B9 IV	3.77	-0.06	-0.08	11.1 \pm 0.1	3.96 \pm 0.25	141
21	55 Cyg	198478	B3 Ia	4.84	0.42	1.11	18.8 \pm 0.3	2.10 \pm 0.13	42
22	β Cep	205021	B1 IV	3.23	-0.22	-0.73	26.8 \pm 0.1	4.12 \pm 0.07	28
23	ζ Peg	214923	B8 V	3.40	-0.08	-0.15	11.4 \pm 0.6	3.89 \pm 0.09	161
24	α Peg	218045	B9 V	2.49	-0.04	-0.03	10.1 \pm 0.1	3.98 \pm 0.25	130
25	105 Aqr	222661	B9.5 V	4.49	-0.04	-0.11	10.9 \pm 0.2	4.30 \pm 0.25	136

Note. Spectral types and magnitudes are taken from SIMBAD. Effective temperatures and gravities are average values taken from the sources listed in Section 2. The projected rotational velocity $v \sin i$ values are from the Catalog of Stellar Rotational Velocities (Głębowski & Gnaniński 2005).

(This table is available in machine-readable form.)

polArimeter (VEGA) beam combiner (Mourard et al. 2009) at the CHARA Array with the purpose of improving the surface brightness—color relation for early-type stars (five of their targets are included here). In addition, there are several studies of individual B-type stars. White et al. (2017) presented interferometric observations of the Pleiades cluster member Maia (HD 23408) that were made with the PAVO beam combiner (including some measurements reported here). Other CHARA targets include the B stars Regulus (McAlister et al. 2005; Che et al. 2011), Rigel (Chesneau et al. 2010), and κ And (Jones et al. 2016), and several B-star targets were observed with the NPOI interferometer (Baines et al. 2018).

Here we present the results of our angular diameter measurements of a sample of 25 B-type stars. Section 2 discusses our interferometric observations, calibration, and data reduction methods. Section 3.1 presents an analysis of the calibrated visibilities to obtain error-weighted fits of the limb-darkened diameters. In Section 3.2, we collect the available flux spectra and make fits of the SED as a function of temperature, angular size, and reddening to compare our observed angular size to model predictions. Section 4 presents a discussion of our results, including the physical radii based on known distances, and comparisons to model predictions and previous interferometric measurements.

2. Observations

Our sample consists of 25 B-type stars with spectral types ranging from B2 to B9.5. All luminosity classes are represented with one supergiant, 14 giants, and 10 main-sequence stars.

The stars are positioned in a decl. range of -14° to $+70^\circ$ and have an apparent magnitude range of $V = 1.6$ – 5 . The targets were selected with a predicted angular diameter of 0.2–1.0 mas. These constraints ensure that our stars have the necessary location, brightness, and angular size to be resolved with the CHARA Array. Three of the targets, Electra (HD 23302), Maia (HD 23408), and Atlas (HD 23850), are members of the Pleiades cluster. A summary of our target stars and their parameters is given in Table 1. Literature values for effective temperature and surface gravity were taken as the average from several sources: the PASTEL catalog (Soubiran et al. 2016), the ELODIE archive (Prugniel & Soubiran 2001), the Indo-US Library (Valdes et al. 2004), the STELIB library (Le Borgne et al. 2003), the MILES library (Cenarro et al. 2007), Cenarro et al. (2001), Gullikson et al. (2016), Kraus et al. (2015), Lyubimkov et al. (2004), Morales et al. (2001), and Zorec et al. (2009).

It is very common for massive stars to be in double or multiple star systems, and several of our sample stars have close, bright companions that need to be considered for interferometric fitting or our spectrophotometric modeling. Table 2 gives a summary of these stars and their companions' properties based on data from the Washington Double Star Catalog⁵ and other sources (final column). The second and third columns of Table 2 give the companion separation in arcseconds and V-band magnitude difference, respectively. Columns 4 and 5 list the effective temperature and surface gravity assumed for the companion. Columns 6 and 7 indicate whether the spectrophotometry or

⁵ <http://ad.usno.navy.mil/wds/>

Table 2
Companions to Target Stars

HD Number	Separation (arcsec)	Δm_V (mag)	Temperature (K)	$\log g$ (c.g.s.)	Spectrophotometric Correction	Interferometric Correction	References
2772	0.42	0.15	10,760	4.3	Y	Y	T00
11502	7.4	-0.06	12,000	4.3	Y	N	WDS
23302	0.2	3.6	8400	4.3	Y	Y	WDS
23850	0.013	1.62	12,200	4.3	Y	Y	Z04
	0.5	3.0	9000	4.3	Y	N	Z04
29763	0.303	2.48	10,500	4.3	Y	Y	B07
	...	1.5	13,000	4.3	Y	N	P61
36267	1.146	1.3	10,500	4.3	Y	Y	F97
155763	0.059	1.03	13,000	4.2	Y	Y	H00
186882	2.51	3.38 ^a	6500	4.3	Y	Y	H99
196867	0.158	2.57	8300	4.6	Y	Y	H99
205021	0.25	3.4	9300	4.3	Y	Y	WDS
222661	5.5	5.42	4800	4.6	Y	N	WDS

Note. B07 = Balega et al. (2007), T00 = ten Brummelaar et al. (2000), F97 = Fu et al. (1997), H00 = Hartkopf et al. (2000), H99 = Horch et al. (1999), P61 = Petrie & Ebbighausen (1961), WDS = Washington Double Star Catalog, Z04 = Zwahlen et al. (2004).

^a H -band $\Delta m = 2.08$ was used for the incoherent flux correction.

interferometry data, respectively, were corrected for the companion flux (Y = yes; N = No).

Observations of our targets were made using the PAVO beam combiner (Ireland et al. 2008) and the CLassic Interferometry with Multiple Baselines (CLIMB) beam combiner (ten Brummelaar et al. 2013) at the CHARA Array (ten Brummelaar et al. 2005), located at Mount Wilson Observatory in California. Combining the longest baseline (331 m) currently available in the world offered by the CHARA Array and the operating wavelength range of the PAVO beam combiner (600–900 nm), we are able to achieve an extremely high angular resolution of about 0.2 mas. The CLIMB beam combiner was used for our larger targets and was operated in the H band (1.67 μm), giving a resolution limit of about 0.5 mas.

The H -band filter used by CLIMB is a wide-band filter with an adopted central wavelength of 1.673 μm . We made an estimate of the centroid of the filtered flux distribution in order to check that observations of hot stars do not skew this central effective wavelength to shorter wavelengths. We used stellar flux distributions from the spectral library of Lancon & Rocca-Volmerange (1992), which spans spectral types from O5V to A3V. We multiplied these spectra by the H -band filter transmission curve, the quantum efficiency curve for the NIRO detector, and the atmospheric transmission curve. The centroid of the resulting distribution was calculated and compared to the adopted central wavelength. We find that the central wavelength for the H band does not vary significantly with the stellar effective temperature. The derived effective wavelength is 1.668 μm , which is only 0.3% different from the adopted wavelength. This is much smaller than other sources of uncertainty in the angular size determination, so we assume that the nominal effective wavelength for the H band is appropriate for all stellar temperatures among the B-type stars. The PAVO beam combiner is a spectrally dispersed combiner with 23 spectral channels. Wavelength calibrations are made for each channel as part of the data reduction process.

Visibility data for each target were collected using the standard “bracket” method in which one bracket is composed of three sets of scans: calibrator—target—calibrator. Calibrators are chosen to be unresolved, single slowly rotating stars that are close to the

target in brightness and position in the sky. These calibrator observations act to rescale the target visibilities for instrumental losses in fringe visibility. Our calibrators are discussed further below.

Observations with the CHARA Array were accomplished from 2012 September to 2017 June over a total of 28 nights of observation. The PAVO observations all used only one baseline, or two telescopes, at a time. Three telescopes were used concurrently for all CLIMB observations. Over the course of the survey, four stars were observed with CLIMB over seven nights, and 21 stars were observed with PAVO over 21 nights.

The data were reduced using the standard data reduction pipelines written for use with the PAVO instrument (Ireland et al. 2008; Maestro et al. 2012) and the CLIMB instrument (ten Brummelaar et al. 2013). The product of both instrumental pipelines is a measurement of squared visibility V^2 as a function of projected baseline or spatial frequency. The closure phase was also measured for the CLIMB three-telescope data, and these measurements were used for the binary fit of HD 23850 discussed in Section 4.2.6.

The target stars have very small angular diameters, so it was difficult to find good calibrators, that is, a similar-magnitude star in close proximity in the sky. The ideal calibrator is small enough to be unresolved by the combiner, because an unresolved target will have a visibility equal to unity for any arbitrarily small angular size. The goal was to observe two calibrators for each target, but in some cases only one was used in practice. The calibrator stars and their angular sizes are given in Table 3. We adopted angular diameters from the JMMC Stellar Diameter Catalog (JSDC⁶) Version 2 (Bourgés et al. 2014; Chelli et al. 2016). The JSDC angular diameters are in good agreement with independent estimates shown in Table 3 but tend to have significantly smaller estimates of uncertainty compared to those given by Swihart et al. (2017).

Table 2 shows which stars have companions close enough and bright enough to require a correction to the visibilities to account for the presence of incoherent flux introduced by the companion. The projected angular separation, difference in magnitude, and seeing estimate during the observation are used to calculate the

⁶ <http://www.jmmc.fr/jsdc>

Table 3
Calibrator Stars

HD Number	Spectral Class	Target Number	JSDC V2 θ_{LD} (mas)	CADARS θ_{LD} (mas)	Swihart et al. (2017) θ_{LD} (mas)
1279	B8 III	2	0.189 ± 0.005	...	0.166 ± 0.040
4142	B5 V	1	0.164 ± 0.005	0.16	0.160 ± 0.034
10982	B9.5 V	3	0.208 ± 0.006	0.19	0.203 ± 0.034
14263	A1 V	4	0.269 ± 0.007	0.29	...
15633	A3 V	4	0.265 ± 0.007
17036	B9 Vn	4	0.218 ± 0.006	0.22	...
18216	B9 V	4	0.145 ± 0.004
19600	A0 V	5	0.176 ± 0.005	0.17	...
23338	B6 IV	7	0.324 ± 0.030	0.33	0.363 ± 0.018
23753	B8 V	7	0.229 ± 0.006	0.22	...
23923	B8 V	5, 6	0.171 ± 0.005	0.18	...
27309	A0 sp	8	0.237 ± 0.006
35600	B9 Ib	9	0.329 ± 0.010	0.28	0.277 ± 0.020
36371	B4 Ib	9	0.401 ± 0.039	0.38	...
36653	B3 V	10	0.149 ± 0.005	...	0.137 ± 0.042
97585	A0 V	11	0.270 ± 0.009	0.25	0.273 ± 0.017
119024	A2 Vnp	12	0.315 ± 0.009	...	0.275 ± 0.028
119124	F7.7 V	12	0.417 ± 0.010
149081	A1 V	13	0.174 ± 0.005
149212	A0 III	14	0.329 ± 0.009	0.35	...
149650	A2 V	13	0.236 ± 0.006	...	0.262 ± 0.012
156295	A7 V	14	0.366 ± 0.011	0.39	0.319 ± 0.008
161693	A2 V	15	0.260 ± 0.008	...	0.267 ± 0.021
167965	B7 IV	15	0.190 ± 0.005	0.18	0.167 ± 0.036
170920	A5 IV/V	17	0.303 ± 0.008
171301	B8 IV	16	0.222 ± 0.006	...	0.189 ± 0.040
178187	A4 III	16	0.281 ± 0.008	...	0.266 ± 0.012
180782	A0 V	18	0.199 ± 0.005
181440	B9 III	18	0.249 ± 0.007
192514	A5 IIIIn	19	0.497 ± 0.036	0.4	0.411 ± 0.060
194012	F7 V	20	0.433 ± 0.011	0.47	...
195556	B2.5 IV	21	0.214 ± 0.008	0.21	0.217 ± 0.050
196724	A0 V	20	0.318 ± 0.027	0.33	0.331 ± 0.020
196740	B5 IV	20	0.215 ± 0.007	0.22	0.245 ± 0.012
197076	G5 V	20	0.459 ± 0.012
197392	B8 II-III	21	0.200 ± 0.005	...	0.174 ± 0.042
203245	B6 V	21	0.166 ± 0.005	0.15	...
204770	B7 V	22	0.218 ± 0.007	0.2	0.192 ± 0.041
207636	A0 V	22	0.166 ± 0.005
216735	A1 V	23, 24	0.322 ± 0.030	0.33	0.368 ± 0.029
217891	B6 Ve	23	0.296 ± 0.009	0.28	0.278 ± 0.059
218700	B9 III	23, 24	0.247 ± 0.007	...	0.227 ± 0.041
218918	A5 Vn	24	0.390 ± 0.033	0.37	0.325 ± 0.028
222847	B9 V	25	0.254 ± 0.007	0.23	...

Note. Target number is the star ID given in Table 1.

intensity for each component assuming a Gaussian profile for the seeing distribution. The squared visibility is then corrected with a scale factor of $(1 + I_{\text{secondary}}/I_{\text{primary}})^2$ (Boyajian et al. 2008), where $I_{\text{secondary}}$ is the flux of the companion that is integrated over the field of view (FOV) of the detector. The FOV corresponds to the size of a pixel projected on the sky for CLIMB (0.808 arcsec per pixel for the NIRO camera) and to the entrance aperture for PAVO (1 arcsec).

Observing data, including dates, baselines, and calibrated visibilities, are given in Table 4. Column 4 of Table 4 lists the spatial frequency of the observation, or the baseline divided by wavelength. Columns 5 and 6 give the positions in the u, v plane of spatial frequency for each observation. Column 8

gives the visibility squared, and column 9 gives the uncertainty associated with each V^2 measurement. Visibilities corrected for companion flux V_C^2 , and their associated uncertainties, are given in columns 10 and 11 of Table 4. The full table is given in the electronic version of the paper.

3. Stellar Parameters

3.1. Interferometry

The visibility data from Table 4 were fit with a limb-darkened, single-star disk model with each point weighted by the inverse square of the error in V^2 . The degree of limb darkening can be measured from the visibility at very high

Table 4
Calibrated Visibilities

HD Number (1)	MJD (2)	Telescope Pair (3)	$10^{-6}B/\lambda$ (rad^{-1}) (4)	u (arcsec^{-1}) (5)	v (arcsec^{-1}) (6)	Baseline (m) (7)	V^2 (8)	ΔV^2 (9)	V_C^2 (10)	ΔV_C^2 (11)
2772	56912	WIS1	312.64	-1270.07	-827.26	236.48	0.290	0.097	0.906	0.097
2772	56912	WIS1	327.40	-1330.03	-866.32	236.48	0.304	0.063	0.947	0.063
2772	56912	WIS1	330.33	-1341.92	-874.06	236.48	0.294	0.066	0.917	0.066
2772	56912	WIS1	333.31	-1354.02	-881.95	236.48	0.310	0.090	0.966	0.090
2772	56912	WIS1	338.94	-1376.92	-896.86	236.48	0.312	0.082	0.975	0.082
2772	56912	WIS1	341.84	-1388.66	-904.51	236.48	0.242	0.053	0.756	0.053
2772	56912	WIS1	344.73	-1400.40	-912.16	236.48	0.235	0.049	0.734	0.049
2772	56912	WIS1	347.56	-1411.93	-919.67	236.48	0.231	0.048	0.721	0.048
2772	56912	WIS1	350.34	-1423.23	-927.02	236.48	0.228	0.059	0.710	0.059
2772	56912	WIS1	353.12	-1434.49	-934.36	236.48	0.241	0.073	0.752	0.073

(This table is available in its entirety in machine-readable form.)

spatial frequencies, but in general our observations record only the lower frequencies in these small targets. Consequently, we set the limb-darkening relations from theoretical models. Linear limb-darkening coefficients were interpolated from the tables from Claret & Bloemen (2011) using the photospheric parameters given in Table 1. These limb-darkening coefficients μ were calculated for model atmospheres that adopt a solar metallicity and a microturbulent velocity of 2 km s^{-1} . A linear limb-darkening law is only a rough approximation of the actual limb-darkening function, but it is sufficient for visibility fits at relatively low spatial frequency. We occasionally encountered calibrated visibilities with an unphysical value greater than unity (for stars close to the resolution limit of the combiner or with poor calibration data). This occurred for only a few stars in our sample ($\sim 5\%$ of sample stars), and these points were rejected from the fitting process.

Visibility curves for each star are shown in Figure Set 1 (given in full in the online version). These portray the calibrated V^2 measurements and the error-weighted fit of all the data with a limb-darkened disk model. The plots show visibilities corrected for the presence of a companion where appropriate (see Table 2).

Table 5 lists the derived uniform disk (UD) and limb-darkened (LD) disk angular diameters θ , the latter calculated for a linear limb-darkening coefficient μ . Errors associated with the angular diameters were calculated from two or three components. The first component was the uncertainty associated with the angular diameter based on the size of the residuals to the fit. The second component reflects the night-to-night variations in the derived stellar angular diameter. We found an internight scatter of $\sigma = 0.052\theta$ for the PAVO data and $\sigma = 0.069\theta$ for the CLIMB data, where σ is the night-to-night standard deviation and θ is the angular diameter in mas. Finally, for B stars whose small angular size, uncorrected for companion flux, was close to that of the calibrator (HD 3360, HD 29763, and HD 36267), we added a third component for the uncertainty because of the error in the assumed calibrator size. We fit the data for these stars after adjusting the calibrator sizes by plus and minus 1σ . We took the half-range between the sizes to represent the result of calibrator uncertainty. The final error estimate is the quadratic sum of the uncertainty from the residuals of the fit, the internight scatter, and, for small stars, the error introduced by the calibrator size. These error estimates are given with the uniform disk and limb-darkened disk diameters in Table 5. We discuss in Section 4.2 several

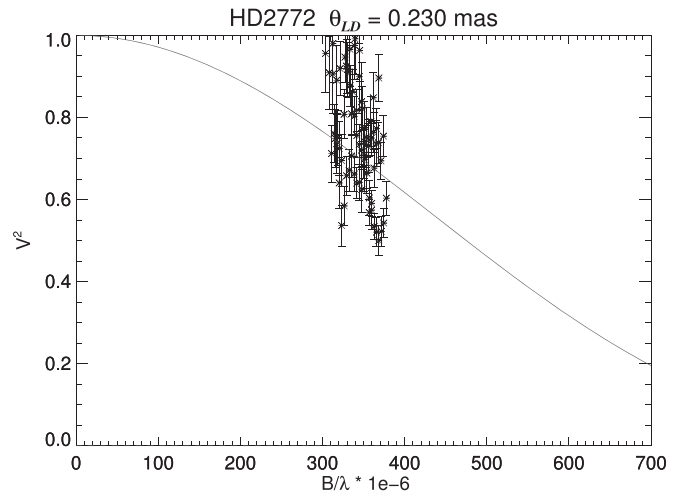


Figure 1. Visibility squared as a function of spatial frequency for CHARA measurements of HD 2772. The solid line shows an error-weighted fit for a limb-darkened, spherical star.

(The complete figure set (25 images) is available.)

problematic cases that are marked with a dagger in the θ_{LD} column of Table 5. The final column in Table 5 gives the maximum ratio of θ_{cal} to θ_{LD} for each target. This is used to highlight those cases where the derived angular size is particularly sensitive to the assumed angular diameter of the calibrator star.

Table 6 gives a comparison of our measured angular diameters to previously estimated values based on SED measurements (see Section 3.2). Our angular diameter measurements are in good agreement with these with the exception of three cases where the observed and SED-implied angular diameters differ by more than 3σ : HD 36267, HD 198478, and HD 205021. All three are cases with complications described in Section 4.2.

3.2. Spectrophotometry

Here we construct fits of the observed SEDs over a grid of effective temperature T_{eff} , angular size θ_{LD} , and reddening $E(B - V)$ using flux predictions from model atmospheres. These fits provide us with estimates of θ_{LD} from the global best fit of the SED, which can be compared with the observed values from our CHARA observations. Conversely, we can use the

Table 5
Observations and Measured Angular Diameters

HD Number (1)	Beam Comb. (2)	Baselines (3)	N_{ν^2} (4)	θ_{UD} (mas) (5)	R Band μ (6)	H Band μ (7)	θ_{LD} (mas) (8)	Maximum $\theta_{cal}/\theta_{target}$ (9)
2772	P	W1S2	115	0.224 ± 0.017	0.36	...	0.230 ± 0.017	0.71
3360	P	E1W1, E1S1	46	0.274 ± 0.018	0.22	...	0.280 ± 0.018^a	0.60
11502	P	E1S1	69	0.336 ± 0.019	0.34	...	0.346 ± 0.019	0.68
15318	P	W1S2, E1S1	91	0.388 ± 0.023	0.33	...	0.400 ± 0.023	0.67
23302	P	E1S1	46	0.472 ± 0.025	0.27	...	0.478 ± 0.025^a	0.37
23408	P	E1S1	46	0.422 ± 0.023	0.32	...	0.436 ± 0.023	0.39
23850	C	E1W1S1	24	0.464 ± 0.043	...	0.16	0.469 ± 0.043^a	0.69
29763	P	E1S1	46	0.220 ± 0.016	0.34	...	0.226 ± 0.016^a	1.05
35497	C	E1W1S1	6	1.074 ± 0.076	...	0.16	1.090 ± 0.076	0.37
36267	P	E1S1	69	0.196 ± 0.015	0.25	...	0.200 ± 0.015^a	0.75
98664	P	E1S1	69	0.452 ± 0.025	0.40	...	0.468 ± 0.025	0.58
120315	C	E1W1S1	28	0.818 ± 0.060	...	0.18	0.834 ± 0.060	0.50
147394	P	E1W1	115	0.354 ± 0.020	0.32	...	0.364 ± 0.020	0.48
155763	P	W1S2	87	0.474 ± 0.026	0.33	...	0.488 ± 0.026^a	0.75
160762	P	E1W1	46	0.326 ± 0.018	0.29	...	0.334 ± 0.018	0.78
176437	P	W2S2	92	0.712 ± 0.038	0.33	...	0.734 ± 0.038	0.38
177756	P	W2S2	106	0.556 ± 0.030	0.32	...	0.570 ± 0.030	0.53
184930	P	E1W1	115	0.328 ± 0.020	0.33	...	0.338 ± 0.020	0.74
186882	C	E1W1S1	9	0.874 ± 0.062	...	0.16	0.884 ± 0.062	0.56
196867	P	E2S2	138	0.407 ± 0.022	0.31	...	0.420 ± 0.022	1.09
198478	P	W1S2, W2S2	161	0.434 ± 0.023	0.36	...	0.448 ± 0.023^a	0.45
205021	P	W1S2	115	0.274 ± 0.016	0.28	...	0.280 ± 0.016^a	0.78
214923	P	E2S2	139	0.551 ± 0.030	0.34	...	0.562 ± 0.030	0.57
218045	P	E2W2, E2S2	312	1.039 ± 0.066	0.34	...	1.052 ± 0.066	0.36
222661	P	E1S1	21	0.338 ± 0.018	0.39	...	0.348 ± 0.018	0.73

Note. Beam Comb. = beam combiner used for observations: P = PAVO, C = CLIMB.

^a Indicates results we consider preliminary for reasons discussed in Section 4.2.

(This table is available in machine-readable form.)

observed angular diameter and the SED fits to find an independent estimate of temperature.

Spectrometry from multiple sources was collected to span the wavelength range from the ultraviolet to infrared (1200 Å to 2 μ m). The sources used include *IUE* (*International Ultraviolet Explorer*) spectra and the Ultraviolet Bright-Star Spectrophotometric Catalog (Jamar et al. 1976) for the near and far UV, Burnashev (1985) and Alekseeva et al. (1996) for the optical range, and 2MASS (Two Micron All Sky Survey, Cutri et al. 2003) and *WISE* (*Wide-field Infrared Survey Explorer*, Cutri et al. 2012) in the IR. *IUE* spectral fluxes were recalibrated with the routine written by Massa & Fitzpatrick (2000). All flux values were assigned a uniform 3% uncertainty to ensure our program fit all parts of the spectrum equally.

The spectra were compared to predictions from the TLUSTY BSTAR2006 (Lanz & Hubeny 2007) or ATLAS9 (Kurucz 1992; Castelli & Kurucz 2004) stellar atmosphere models. Both the TLUSTY and ATLAS9 models assume solar abundances and a microturbulent velocity of $v_t = 2 \text{ km s}^{-1}$. Stars with effective temperatures above 17,000 K were fit with the TLUSTY BSTAR2006 models (which include non-LTE effects that become more important in hotter atmospheres), while stars under 17,000 K were fit with the ATLAS9 models. Stars around the boundary temperature range between models were fit with both models to ensure good agreement.

Model spectra were constructed for each grid value of T_{eff} , θ_{LD} , $E(B - V)$, and $\log g$ (from the average of literature values given in Table 1) following the procedures outlined in our prior paper (Gordon et al. 2018). Model and observed spectra were

rebinned to a resolving power of $R = 60$ to ensure the fit was not dominated by any wavelength range with a larger number of measurements. In cases where there was a close, bright companion (Table 2), the extra flux from the companion was added to the model spectrum. The values of T_{eff} and $\log g$ for the companion were used to calculate its spectrum in the same way using the ATLAS9 models (Kurucz 1992; Castelli & Kurucz 2004). The companion flux was then rescaled according to the V -band magnitude difference Δm_V (Table 2), with the relation $\frac{f_c}{f_p} = 10^{-0.4\Delta m_V}$, and then added to the model flux calculated for the primary to form a composite spectrum.

For each grid pair of assumed (θ_{LD} , T_{eff}), model spectra were formed over a range of reddening, and the best-fit value $E(B - V)$ and minimum χ_ν^2 were saved in matrices. Contour maps were created by plotting the χ_ν^2 matrix as a function of effective temperature and angular size for each star, and these are shown in Figure Set 2 (given in full in the online version). Overplotted are vertical lines showing the angular size obtained from our interferometry with a 1σ margin, and horizontal lines showing the average literature temperature (Table 1) with a 1σ margin.

We located the position of the global minimum χ_ν^2 in the diagrams of Figure Set 2. The angular diameter corresponding to the global minimum χ_ν^2 is listed in the final column of Table 6 under the heading SED (discussed in Section 4.1). The temperature of the global minimum is likewise given as $T_{\text{eff}}(\text{SED})$ in column 3 of Table 7.

Table 6
Comparison of Observed and Literature Angular Diameter Measurements

HD Number (1)	This Work θ_{LD} (mas) (2)	JSDC V2 θ_{LD} (mas) (3)	Underhill θ_{LD} (mas) (4)	CADARS θ_{LD} (mas) (5)	Swihart θ_{LD} (mas) (6)	SED θ_{LD} (mas) (7)
2772	0.230 ± 0.017	0.29	...	0.218 ± 0.080
3360	0.280 ± 0.018^a	0.297 ± 0.031	0.303 ± 0.002	0.27	0.319 ± 0.013	0.304 ± 0.010
11502	0.346 ± 0.019	0.40	...	0.398 ± 0.019
15318	0.400 ± 0.023	0.372 ± 0.032	...	0.42	0.387 ± 0.058	0.421 ± 0.010
23302	0.478 ± 0.025^a	0.418 ± 0.043	...	0.40	...	0.445 ± 0.007
23408	0.436 ± 0.023	0.453 ± 0.043	...	0.43	0.410 ± 0.099	0.460 ± 0.040
23850	0.469 ± 0.043^a	0.495 ± 0.053	...	0.80	...	0.469 ± 0.030
29763	0.226 ± 0.016^a	0.133 ± 0.004	...	0.27	...	0.245 ± 0.005
35497	1.090 ± 0.076	1.155 ± 0.097	1.065 ± 0.010	1.10	...	1.130 ± 0.005
36267	0.200 ± 0.015^a	0.40	...	0.270 ± 0.010
98664	0.468 ± 0.025	0.429 ± 0.044	...	0.45	0.418 ± 0.075	0.466 ± 0.018
120315	0.834 ± 0.060	0.772 ± 0.091	0.826 ± 0.006	0.84	0.670 ± 0.141	0.835 ± 0.020
147394	0.364 ± 0.020	0.387 ± 0.032	0.358 ± 0.001	0.37	...	0.370 ± 0.015
155763	0.488 ± 0.026^a	0.514 ± 0.047	0.586 ± 0.003	0.59	...	0.461 ± 0.010
160762	0.334 ± 0.018	0.310 ± 0.029	0.332 ± 0.003	0.34	...	0.332 ± 0.010
176437	0.734 ± 0.038	0.730 ± 0.083	...	0.75	0.647 ± 0.117	0.720 ± 0.070
177756	0.570 ± 0.030	0.605 ± 0.062	0.563 ± 0.002	0.56	0.565 ± 0.085	0.567 ± 0.030
184930	0.338 ± 0.020	0.334 ± 0.033	0.322 ± 0.003	0.35	...	0.340 ± 0.005
186882	0.884 ± 0.062	0.86	0.831 ± 0.050	0.834 ± 0.110
196867	0.420 ± 0.022	...	0.531 ± 0.006	0.51	...	0.464 ± 0.030
198478	0.448 ± 0.023^a	0.416 ± 0.040	0.531 ± 0.003	0.44	...	0.530 ± 0.013
205021	0.280 ± 0.016^a	0.094 ± 0.003	0.309 ± 0.004	0.30	...	0.340 ± 0.010
214923	0.562 ± 0.030	0.576 ± 0.054	...	0.55	0.545 ± 0.093	0.578 ± 0.040
218045	1.052 ± 0.066	0.899 ± 0.093	...	0.94	0.975 ± 0.059	1.000 ± 0.100
222661	0.348 ± 0.018	0.387 ± 0.045	...	0.36	0.349 ± 0.052	0.370 ± 0.040

Note. JSDC = JMMC Stellar Diameters Catalog V2, Bourgés et al. (2014); Underhill = Underhill et al. (1979); CADARS = Pasinetti Fracassini et al. (2001); Swihart = Swihart et al. (2017); SED = angular diameter associated with the global minimum of χ^2_ν of the model fit of the SED.

^a Indicates results we consider preliminary for reasons discussed in Section 4.2.

(This table is available in machine-readable form.)

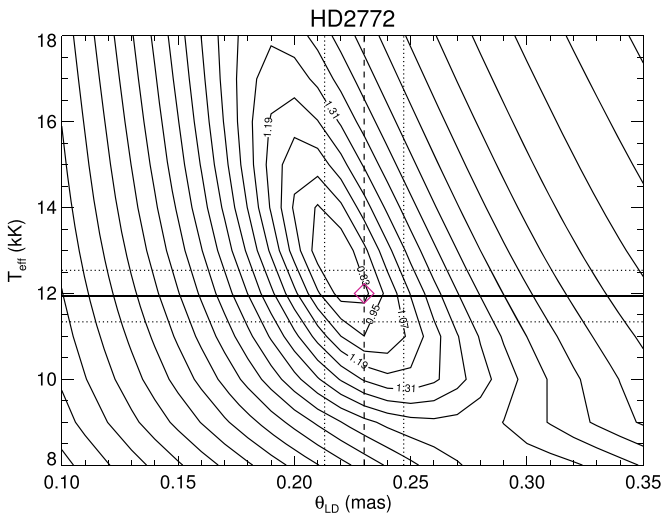


Figure 2. Contour map of χ^2_ν differences between the ATLAS9 model and observed fluxes for the best-fit reddening as a function of limb-darkened angular size and effective temperature for HD 2772. Overplotted are vertical lines showing angular size obtained from our interferometry and horizontal lines showing the average temperature from the literature. Dotted lines show an error margin of $\pm 1\sigma$ for the angular size and average temperature. The diamond symbol indicates the best-fit model temperature for our directly determined angular size.

(The complete figure set (25 images) is available.)

We derived another temperature estimate by locating the position in the χ^2_ν diagram where the vertical line marking the observed angular size crossed the lowest value of χ^2_ν . A diamond symbol indicates this best-fit temperature in the plots of Figure Set 2, and these T_{\min} estimates are listed as $T_{\text{eff}}(\theta_{LD})$ in column 2 of Table 7. Uncertainties were found by renormalizing the set of χ^2_ν values to the minimum χ^2_ν and fitting the $(T_{\text{eff}} - T_{\min}, \chi^2_\nu)$ points with a parabolic curve. The temperature uncertainty was then taken as the half-range between points on the curve with a reduced χ^2_ν equal to $\left(1 + \frac{1}{(N_{\text{points}} - \text{DoF})}\right)$, where N_{points} is the number of spectral data points in the fit, and the degrees of freedom (DoF) was set to three (for fitting parameters T_{eff} , θ_{LD} , and $E(B - V)$). Note that this uncertainty does not account for the error in θ_{LD} and the subsequent change in the best-fit T_{eff} over the possible range in θ_{LD} . However, inspection of the χ^2_ν diagrams in Figure Set 2 demonstrates for each case how the best-fit T_{eff} changes (often by a large amount) over the range of $\pm \Delta\theta_{LD}$.

We used the $(\theta_{LD}(\text{obs}), T_{\min})$ coordinate for the temperature associated with the observed angular diameter to extract a corresponding estimate of reddening from the best-fit $E(B - V)$ matrix. These reddening estimates are listed in column 5 of Table 7, along with comparisons to previously determined values.

Table 7
Temperature and Reddening Estimates

HD Number (1)	Derived $T_{\text{eff}}(\theta_{\text{LB}})$ (kK) (2)	SED $T_{\text{eff}}(\text{SED})$ (kK) (3)	Literature $T_{\text{eff}}(\text{Lit})$ (kK) (4)	Best Fit $E(B - V)$ (mag) (5)	Literature $E(B - V)$ (mag) (6)
2772	12.0 ± 0.5	12.8 ± 0.5	11.9 ± 0.6	0.024	0.02
3360	24.5 ± 0.8^a	21.5 ± 0.8	21.5 ± 0.5	0.061 ^a	0.05
11502	11.0 ± 1.1	9.5 ± 1.0	10.0 ± 1.0	0.048	0.04
15318	11.1 ± 1.4	11.0 ± 1.0	10.6 ± 1.0	0.036	0.03
23302	14.7 ± 0.8^a	14.7 ± 0.8	14.7 ± 1.0	0.124 ^a	0.05
23408	14.7 ± 0.9	14.7 ± 0.9	13.8 ± 1.0	0.152	0.04
23850	13.5 ± 0.3^a	13.5 ± 0.3	13.0 ± 1.0	0.114 ^a	0.04
29763	18.5 ± 0.8^a	17.0 ± 0.8	16.6 ± 1.0	0.048 ^a	0.08
35497	14.0 ± 1.1	14.0 ± 1.0	13.6 ± 0.1	0.043	0.01
36267	... ^a	15.7 ± 0.5	16.3 ± 0.7	... ^a	0.03
98664	11.1 ± 1.4	11.0 ± 1.0	10.5 ± 0.1	0.067	0.03
120315	17.0 ± 0.9	17.0 ± 0.9	17.7 ± 0.3	0.007	0.03
147394	16.9 ± 0.7	16.9 ± 0.7	15.4 ± 0.7	0.050	0.02
155763	15.0 ± 0.8^a	15.0 ± 0.8	13.5 ± 0.8	0.064 ^a	0.03
160762	18.2 ± 0.7	18.2 ± 0.7	18.2 ± 1.0	0.036	0.03
176437	11.0 ± 1.4	11.0 ± 1.0	10.4 ± 0.6	0.133	0.04
177756	12.0 ± 1.3	12.0 ± 1.0	10.7 ± 1.0	0.048	0.02
184930	14.5 ± 0.6	14.5 ± 0.6	13.9 ± 0.5	0.095	0.10
186882	12.0 ± 1.4	12.0 ± 1.0	10.4 ± 0.4	0.190	0.01
196867	13.3 ± 1.3	13.3 ± 1.3	11.1 ± 0.1	0.107	0.02
198478	18.8 ± 1.4^a	16.5 ± 1.0	18.8 ± 0.3	0.679 ^a	0.53
205021	29.5 ± 2.5^a	23.6 ± 1.0	26.8 ± 0.1	0.067 ^a	0.05
214923	12.3 ± 1.4	12.3 ± 1.0	11.4 ± 0.6	0.057	0.04
218045	10.0 ± 1.0	10.0 ± 1.0	10.1 ± 0.1	0.057	0.04
222661	11.0 ± 1.3	11.0 ± 1.3	10.9 ± 0.2	0.024	0.01

Note. Literature $E(B - V)$ values are the average from Neckel et al. (1980) and Savage et al. (1985).

^a Indicates results we consider preliminary for reasons discussed in Section 4.2.

(This table is available in machine-readable form.)

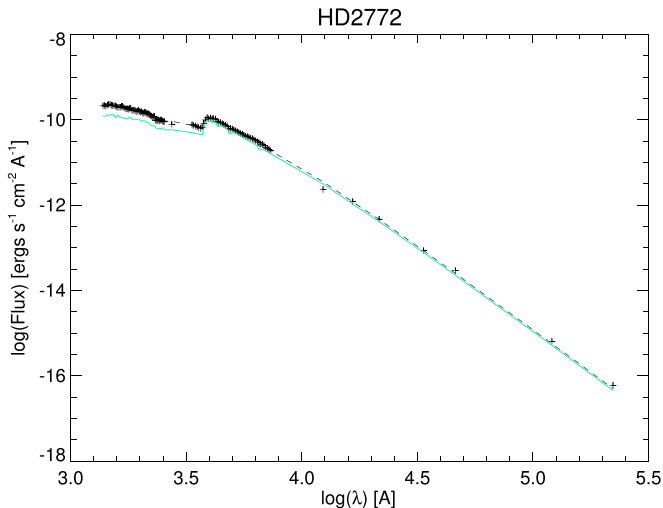


Figure 3. Spectral energy distribution for HD 2772. The plus signs show the collected spectral fluxes. The solid green line shows the SED derived from our interferometric size and best-fit temperature and reddening. The dashed line indicates the SED derived from the temperature and angular size predicted by the model at the global minimum in the χ^2_{ν} diagram.

(The complete figure set (25 images) is available.)

SEDs for each target B star are shown in Figure Set 3 (given in full in the online version). The symbols represent the spectral data used in the fits, and the solid green line shows the SED

constructed using the interferometric size and best-fit temperature T_{min} and corresponding reddening. For comparison, the dashed black line shows the SED derived from the model for the angular size and temperature at the global minimum in the χ^2_{ν} diagrams.

4. Discussion

4.1. Stellar Radii and Temperatures

The new angular diameter measurements presented here appear to be consistent with earlier interferometric observations. A comparison of our angular diameter measurements to previous ones is shown in Figure 4. These include measurements from Challouf et al. (2014), Maestro et al. (2013), White et al. (2017), and Hanbury Brown et al. (1974). There is good agreement between measurements from different interferometers and beam combiners (with a few exceptions discussed in Section 4.2). Consequently, our results extend the earlier results in a consistent and reliable way.

The angular diameters derived from the global best fit of the SED are in reasonably good agreement with our directly measured angular diameters. Figure 5 shows a comparison of the observed and SED-derived angular diameters together with a line of slope unity. The error-weighted average ratio is $\langle \theta_{\text{model}} / \theta_{\text{obs}} \rangle = 1.039 \pm 0.016$ (shown as a dotted line), which might indicate that the models lead to an overestimate of the diameters. However, several of the stars with only preliminary results (such as the supergiant 55 Cyg (HD 198478) discussed

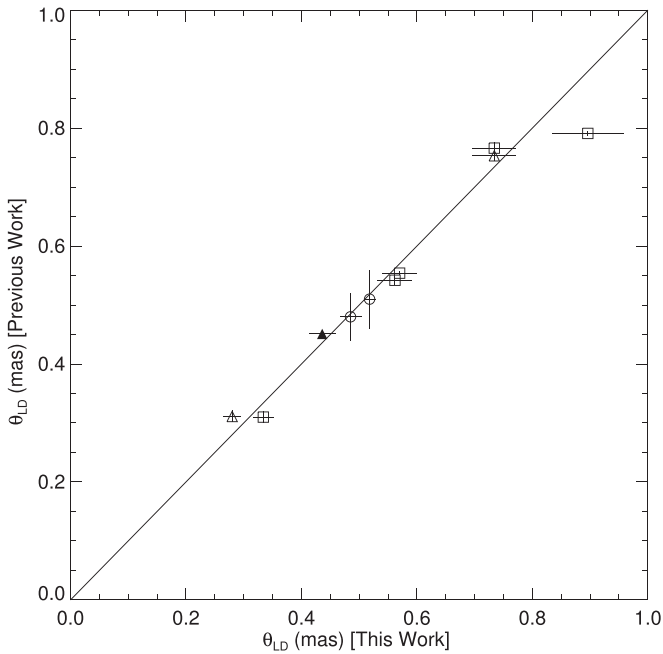


Figure 4. Comparison of our measured θ_{LD} to previous work. Squares = VEGA observations by Challouf et al. (2014), open triangles = PAVO observations by Maestro et al. (2013), filled triangle = PAVO observation by White et al. (2017), circles = NSII observations by Hanbury Brown et al. (1974).

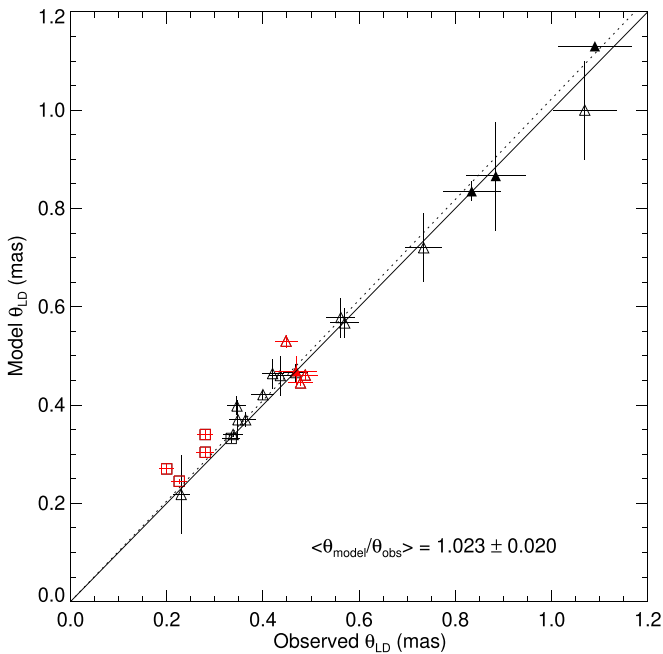


Figure 5. Comparison of our observed angular diameters (column 8 of Table 5) to the SED-derived model size (column 7 of Table 6). The solid line is a unit-slope line for reference, and the dotted line indicates the weighted mean of $\theta_{model}/\theta_{obs}$. Square symbols indicate stars fit with the TLUSTY BSTAR2006 models, triangles indicate stars fit with ATLAS9 models, and filled triangles indicate stars fit with CLIMB data. Red points are measurements considered preliminary and are not included in the weighted mean ratio shown.

in Section 4.3.1) appear farthest from the unit slope line, and the average ratio after deletion of the preliminary sample yields $\langle \theta_{model}/\theta_{obs} \rangle = 1.023 \pm 0.020$, only a marginal difference. Thus, the model fits of the SED generally imply angular diameters that are consistent with the observations.

Next we consider estimates of T_{eff} from the global fit and angular size restricted fit of the SED. The left panel of Figure 6 shows this comparison together with a reference line of slope unity. The error-weighted average ratio of the whole sample is $\langle T_{eff}(SED)/T_{eff}(\theta_{LD}) \rangle = 0.971 \pm 0.015$, but the fit is affected by deviations in estimates from the preliminary cases (such as those for the hot stars HD 3360 and HD 205021). Removing the preliminary results from the sample yields $\langle T_{eff}(SED)/T_{eff}(\theta_{LD}) \rangle = 1.004 \pm 0.022$. Thus, consistency between the SED-derived and observed angular sizes (Figure 5) leads to agreement in the temperature estimates because $T_{eff}(\theta_{LD})$ is derived from the local best fit of the SED along a line of constant θ_{LD} (Section 3.2).

The estimates of $T_{eff}(Lit)$ that are primarily based on spectral line studies do show some differences from those derived from the SED. The right-hand panel of Figure 6 shows a comparison of T_{eff} estimates from the literature compilation (Table 1, column 8 and Table 7, column 4) with those from fits of the SED fixed at the observed angular size (Table 7, column 2). The error-weighted average ratio is $\langle T_{eff}(Lit)/T_{eff}(\theta_{LD}) \rangle = 0.938 \pm 0.015$ for the whole sample and is 0.957 ± 0.022 after removal of the preliminary results. The latter represents a 2σ smaller estimate for T_{eff} from line studies compared to that from the continuum SED fit at the observed angular size.

We can combine our observed angular diameters with known distances to calculate stellar radii. Table 8 lists distance estimates from three sources and the derived stellar radii. The distance d_1 is based on spectral diagnostics reported by Underhill et al. (1979). The next d_2 is derived from the *Hipparcos* parallax (van Leeuwen 2007). The third estimate d_3 is from *Gaia* DR2 parallaxes (Gaia Collaboration et al. 2018). The last column gives the calculated stellar radius from $R/R_{\odot} = d(\text{pc}) \times \theta_{LD}(\text{mas})/9.30$. The radius value is based on the *Gaia* DR2 distance where available and our measured angular diameter. If no *Gaia* DR2 parallax is available, then the *Hipparcos* value is adopted. The DR2 listing for HD 205021 is likely incorrect as this star has a known speckle companion (Wheelwright et al. 2009) and the *Gaia* DR2 analysis does not yet account for stellar companions. For this reason we have adopted the parallax of the B component for this star.

We used our derived estimates for stellar radius and effective temperature to place the stars on an observational HR diagram that is shown in Figure 7 and includes both the O-star (Gordon et al. 2018) and B-star samples. Circles indicate the O stars, while the triangles mark the two O stars for which we only have upper or lower limits on T_{eff} . Overplotted are evolutionary tracks and isochrones for the MESA grid (Paxton et al. 2013; Choi et al. 2016; Dotter 2016). The models chosen are for nonrotating stars and solar metallicity. These show evolutionary tracks for stellar masses of $2.5 M_{\odot}$, $5 M_{\odot}$, $10 M_{\odot}$, $20 M_{\odot}$, and $40 M_{\odot}$ and isochrones for ages of 1 Myr, 3.2 Myr, 10 Myr, and 32 Myr. Pre-main-sequence and evolutionary endpoint sections of the tracks have been omitted for clarity.

Two of the O stars are members of stellar clusters or associations, and these can provide an independent check of stellar age. λ Ori (HD 36861) is a member of the Collinder 69 cluster, which has an estimated age of 5 Myr (Wu et al. 2009). ζ Ori A (HD 37742) is a member of the Ori OB1b association, which has an estimated age of 4 Myr (Kounkel et al. 2018). Both of these stars are located in Figure 7 at coordinates that approximately agree with these age estimates. There are three members of the Pleiades star cluster in the B-star sample: Electra (HD 23302), Maia (HD 23408), and Atlas (HD 23850).

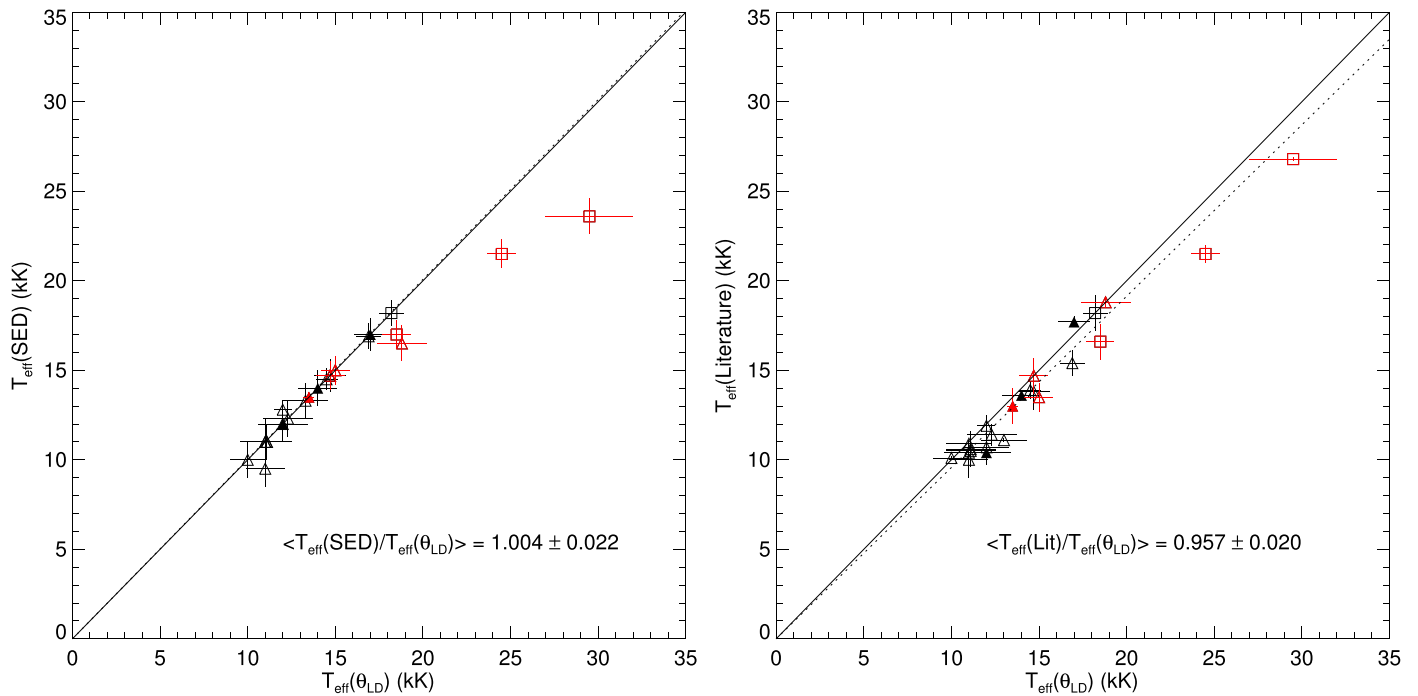


Figure 6. The left panel shows a comparison of the model effective temperatures $T_{\text{eff}}(\text{SED})$ (Table 7, column 3) and our derived effective temperatures $T_{\text{eff}}(\theta_{\text{LD}})$ (Table 7, column 2). The right panel shows a comparison of our derived temperatures to the average literature temperature $T_{\text{eff}}(\text{Lit})$ (Table 7, column 4). In both plots, the solid line is a unit line for reference, and the dotted line indicates the weighted mean of the ratio of variables being compared. Square symbols indicate stars fit with the TLUSTY BSTAR2006 models, triangles indicate stars fit with ATLAS9 models, and filled triangles indicate stars fit with CLIMB data. Red points are measurements considered preliminary and are not included in the weighted mean ratios shown.

Recent calculations by Gossage et al. (2018) yield an estimated age of 110–160 Myr for the Pleiades. Our parameters for these three stars result in an age estimate that is approximately the same.

4.2. Notes on Individual Stars

4.2.1. HD 2772

λ Cas (HD 2772) has a bright nearby companion, so the binary corrections are sensitive to the adopted magnitude difference. The SED fit (Figure 3.1) in the UV is much better for the global solution than that with fixed θ_{LD} , which is probably a consequence of a poor binary flux correction.

4.2.2. HD 3360

ζ Cas (HD 3360) was previously observed with the PAVO beam combiner by Maestro et al. (2013). They obtained two brackets of data on a single baseline (S1E1) and obtained a limb-darkened diameter of 0.311 ± 0.010 mas. This is 11% larger than our measured diameter at 0.280 ± 0.015 mas. We also obtained two brackets of data on this star but on two different baselines (S1E1 and E1W1). ζ Cas is not a rapid rotator, with a $v \sin i$ of only 17 km s^{-1} (Table 1), so we should not be observing any rotational distortion on different baselines. However, our measured sizes on different baselines differed by about 10%. Maestro et al. (2013) also used the same calibrator for their observations as ours, HD 1279, but adopted a larger angular size of 0.202 mas. This could explain the larger angular size they measure for ζ Cas. Our results are preliminary because of the uncertainty associated with the calibrator diameter.

4.2.3. HD 11502

HD 11502, or γ^1 Ari, is a binary star system with a very similar companion. This companion, γ^2 Ari, is an A2 IVp star 7.4 arcsec away and with $\Delta m_V = -0.06$ mag. Due to their similarity, there has been confusion over which star is labeled HD 11502. SIMBAD assigns γ^1 Ari to the more northerly and slightly fainter star of the pair, which is the target we observed. All of the optical spectral sources we found included the spectra of both stars in the pair. However, the UV spectral fluxes are associated with γ^1 Ari alone. We chose to use only the optical spectral data for our spectrophotometric fitting with a binary model. The χ^2_ν and SED plots relate to only the fitted optical spectrum.

4.2.4. HD 23302

Electra (HD 23302) is a member of the Pleiades cluster. The spectrum occasionally displays hydrogen emission lines (Be spectrum) from a circumstellar disk. The BeSS database (<http://basebe.obspm.fr/basebe/>) maintains a catalog of spectra of Be stars. At the time of our observations, 2013 December, Electra showed evidence for the presence of a small disk in the weak emission filling of the $H\alpha$ core. The presence of a disk implies that our angular diameter may be slightly overestimated. However, Electra was observed with PAVO in the R band, where any flux contribution from the disk will be small. We consider our result preliminary because of the potential influence of the disk on the measurements.

4.2.5. HD 23408

Maia (HD 23408) is another Pleiades member. A companion is listed in the Washington Double Star Catalog from a lunar occultation observation with a small separation and $\Delta m_V = 1$.

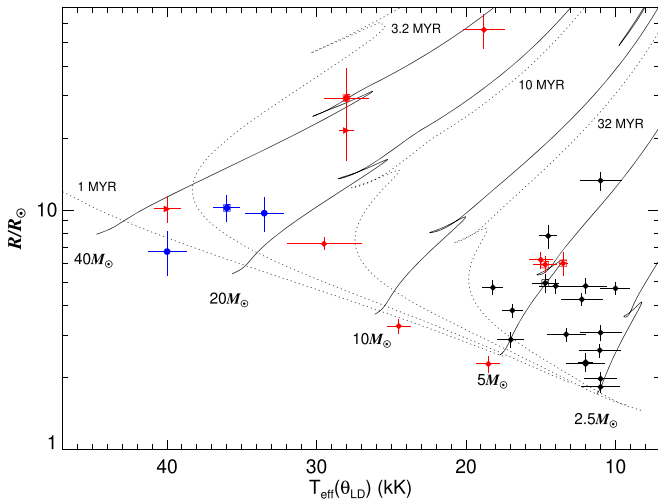


Figure 7. Observational HR diagram for our targets based on our observed diameters and derived effective temperatures. The black diamonds indicate B stars, blue circles O stars, and triangles are O stars with only upper or lower effective temperature estimates. Red points indicate results we consider to be preliminary. Symbols enclosed by squares indicate stars that are cluster members. Evolutionary tracks and isochrones are from the MESA grid.

Table 8
Distance and Radius Estimates

HD Number	d_1 (pc)	d_2 (pc)	d_3 (pc)	R (R_\odot)
2772	...	115.7 ± 5.8	93.6 ± 4.0	2.31 ± 0.20^a
3360	179	181.8 ± 5.3	108.8 ± 4.0	3.28 ± 0.24^b
11502	...	50.3 ± 2.4	53.0 ± 1.2	1.97 ± 0.12^a
15318	...	59.2 ± 4.2	60.4 ± 1.7	2.60 ± 0.17
23302	...	124.1 ± 3.8	114.9 ± 6.9	$5.91 \pm 0.47^{a,b}$
23408	...	117.5 ± 3.9	105.5 ± 7.6	4.95 ± 0.44
23850	...	117.2 ± 5.4	118.6 ± 7.8	$5.98 \pm 0.67^{a,b}$
29763	...	122.1 ± 13.1	93.4 ± 5.2	$2.27 \pm 0.20^{a,b}$
35497	37	41.1 ± 0.6	...	4.82 ± 0.34
36267	...	92.9 ± 5.5	108.4 ± 8.2	$2.33 \pm 0.25^{a,b}$
98664	...	67.5 ± 1.1	61.0 ± 3.2	3.07 ± 0.23
120315	39	31.9 ± 0.2	...	2.86 ± 0.21
147394	102	94.3 ± 1.0	97.1 ± 3.3	3.80 ± 0.25
155763	98	100.7 ± 3.5	118.0 ± 6.8	$6.19 \pm 0.49^{a,b}$
160762	145	139.5 ± 2.5	132.0 ± 6.3	4.74 ± 0.34
176437	...	190.1 ± 9.8	168.2 ± 11.7	13.28 ± 1.15
177756	42	37.9 ± 0.9	37.0 ± 0.7	2.27 ± 0.13
184930	123	119.9 ± 11.4	214.4 ± 21.1	7.79 ± 0.89
186882	...	50.6 ± 1.2	...	4.81 ± 0.36^a
196867	62	77.8 ± 2.7	66.8 ± 2.4	3.02 ± 0.19^a
198478	1072	714.3 ± 86.7	1177.0 ± 186.8	56.70 ± 9.46^b
205021	231	210.1 ± 13.2	239.8 ± 1.7	$7.22 \pm 0.42^{a,b}$
214923	...	62.7 ± 0.7	70.0 ± 1.8	4.23 ± 0.25
218045	...	40.8 ± 0.3	...	4.62 ± 0.29
222661	...	45.5 ± 0.5	48.6 ± 0.8	1.82 ± 0.10^a

Notes. Distance references: 1. Underhill et al. (1979), 2. van Leeuwen (2007) and Maíz Apellániz et al. (2008), 3. Gaia Collaboration et al. (2018). Stellar radii are calculated from the *Gaia* DR2 parallaxes where available; *Hipparcos* parallaxes were adopted if no *Gaia* DR2 parallax was available.

^a Indicates stars with close companions (Table 2).

^b Indicates results we consider preliminary for reasons discussed in Section 4.2.

(This table is available in machine-readable form.)

However, in a recent study by White et al. (2017), no companion was considered for their interferometric and photometric fitting. They found an angular diameter of

0.451 ± 0.006 mas ($\sim 3\%$ larger than our size). Our spectrophotometric fitting also works well without the need of flux from a companion. White et al. (2017) found that Maia has a large chemical spot on its surface, and it is possible that the spot flux gave the appearance of a companion in the occultation observation. Consequently, we decided to exclude any companion corrections in the analysis.

4.2.6. HD 23850

Atlas (HD 23850) is a triple system in the Pleiades. There is a close spectroscopic binary companion with a period of 290.81 days (Pan et al. 2004; Zwahlen et al. 2004). There is another farther companion at $0''.5$ with $\Delta m_V = 3.0$. The fit of the spectrophotometry included the flux contributions of both known companions.

The data for Atlas on two nights of observation (2014 September 24 and 2015 September 13) were fit with a grid search binary model fitting routine (Schaefer et al. 2016). The predicted binary separation for each night of data was set based on the orbit derived by Zwahlen et al. (2004). The fitted angular diameters are $\theta_{UD} = 0.431 \pm 0.027$ mas and $\theta_{UD} = 0.497 \pm 0.027$ mas for the two nights, respectively. The average of these values gives our fitted diameter of $\theta_{UD} = 0.464 \pm 0.043$, where the uncertainty is the quadratic sum of half the difference between the two measurements and the average fitting error.

4.2.7. HD 29763

HD 29763, or τ Tau, is a spectroscopic binary with a more distant visual companion. The spectroscopic binary has a 2.9 day orbit, and the close companion contributes 25% of the flux to the system (Petrie & Ebbighausen 1961). However, there is no visual binary orbit for the close pair, and our data are too sparse to solve for these parameters. Therefore, we made no correction to our visibility measurements for the close companion of τ Tau, and the results are preliminary because of the neglect of the close component. The spectrophotometry fit was made with a model for both known companions.

4.2.8. HD 35497

β Tau (HD 35497) is a HgMn star. There is a companion listed in the Washington Double Star Catalog with a separation of $0''.1$ and $\Delta m_V = 0$. However, this lunar occultation result was never subsequently confirmed. Consequently, we have not included a companion in our analysis for β Tau. However, Adelman et al. (2006) find that β Tau is a single lined spectroscopic binary, which implies that the companion is significantly fainter than the primary and should not significantly affect our results.

4.2.9. HD 36267

SED fitting with the observed diameter was not successful for HD 36267, so no fitted values for temperature or reddening are given in Table 7 for this star. HD 36267 is a probable triple system with an inner spectroscopic binary with a period of 3.964 days (Morrell & Levato 1991). It has a farther companion that is listed in Table 2 and was taken into account for the interferometric and spectrophotometric fitting. However, no correction was made for the possible inner pair, and this may be affecting the fit of the SED. HD 36267 is also one of the

smallest B stars in our sample, and the visibility data are noisy. We consider this result preliminary given these complications.

4.2.10. HD 155763

HD 155763 has a close, bright companion with a separation of $0''.059$ and $\Delta m_V = 1.03$. We made some example binary fits of the PAVO visibility data that suggest that the separation is large enough that the companion's flux adds incoherently as assumed. We also obtained some CLIMB data (not reported here) on one night (2015 August 14) that we fit using a grid search binary model (Schaefer et al. 2016). The fit resulted in a primary diameter of 0.494 mas, which is consistent with the PAVO result of 0.488 ± 0.026 mas. This should be considered a preliminary result given the proximity and brightness of the companion.

4.2.11. HD 176437

γ Lyr (HD 176437) was previously observed with the PAVO beam combiner by Maestro et al. (2013). They obtained seven brackets (161 visibility points) on three different baselines (W1W2, W2E2, S1W2). They measure a limb-darkened angular diameter of 0.753 ± 0.009 mas. This is the same within errors as our measured angular diameter of 0.734 ± 0.038 mas. We obtained four brackets of data (92 visibility points) on a single baseline (W2S2).

4.3. HD 184930

There is a large discrepancy (roughly a factor of two) between the *Hipparcos* and *Gaia* DR2 parallaxes for HD 184930. We have been unable to find a reason for this difference, such as the presence of a companion. The adopted radius given in Table 8 is derived using the *Gaia* DR2 parallax. If the *Hipparcos* parallax were used instead, HD 184930 would have a smaller size of $4.4 R_\odot$.

4.3.1. HD 198478

HD 198478, or 55 Cyg, is the only supergiant in our sample. It was observed over two nights with CHARA on different, but similar, baselines. The observed angular size, at 0.448 ± 0.023 mas, is 15% smaller than the model prediction, 0.530 ± 0.013 mas. This, in turn, leads to a best-fit temperature of 18.8 ± 1.4 kK, which is 14% higher than the model fit value of 16.5 ± 1.0 kK. The SED of 55 Cyg was fit with both the ATLAS9 and BSTAR2006 models, and the results showed good mutual agreement.

In a recent study by Kraus et al. (2015), spectra of 55 Cyg were modeled with the FASTWIND code (Santolaya-Rey et al. 1997; Puls et al. 2005) to search for photospheric variability and mass loss variability in the stellar wind. FASTWIND is a non-LTE, spherically symmetric stellar atmosphere code. It includes line-blanketing effects and calculates the structure of the photosphere and the stellar wind. Using this modeling method and their observed spectra, Kraus et al. (2015) found an effective temperature for 55 Cyg of 18.8 kK and a stellar radius of $57 R_\odot$. This translates to an angular diameter of 0.74 mas using their assumed distance of 714 pc. However, the recent *Gaia* DR2 parallax (Gaia Collaboration et al. 2018) puts it at a distance of 1177 ± 187 pc. This distance results in an angular size of 0.45 ± 0.07 mas, which is in good agreement with our measured diameter. Thus, the temperature and stellar radius

derived by Kraus et al. (2015) are in excellent agreement with our best-fit temperature and interferometric observations.

Nevertheless, this higher temperature and smaller angular size do not make an adequate fit of the SED (Figure 3.21). We suspect that part of the problem is the neglect of stellar winds in the TLUSTY BSTAR2006 and ATLAS9 models. It will be important to compare interferometric results and fluxes of the supergiants to models like CMFGEN (Hillier & Miller 1998) that do include the wind extension. Thus, we consider our present result as preliminary.

4.3.2. HD 205021

β Cep (HD 205021) is the prototype variable star for a class of rapid pulsators. It has a companion at $0''.25$ that is a Be star (discussed in Wheelwright et al. 2009). The flux from the disk may cause the companion to be redder than expected, and this may cause the SED fit to be incorrect for the companion correction. Thus, our results are preliminary. In a spectropolarimetry study, Henrichs et al. (2013) suggest a stellar radius of $6.5 R_\odot$, which gives an angular diameter of 0.25 mas at the *Gaia* DR2 distance of 240 pc. This is in reasonable agreement with our measured angular size of 0.280 ± 0.016 .

4.4. Conclusions

Our survey of the angular diameters of 25 B-type stars more than doubles the sample of measured stars in this class. Combining the angular diameters with new parallaxes from *Gaia* DR2 leads directly to estimates of their physical radii with accuracies of about 7%. We also collected spectral fluxes from the UV to IR to explore model fits of the SED that depend primarily on angular diameter, effective temperature, and reddening. When we set aside some of the preliminary results with complications, we find that the interferometric angular diameters and predicted model diameters are in good agreement. This agreement confirms the validity of the application of the TLUSTY and ATLAS9 stellar atmosphere models for most main-sequence B-type stars, although a complete characterization of other stellar parameters (gravity, microturbulent velocity, and abundance) remains to be explored (Fitzpatrick & Massa 1999).

There are, however, a number of discrepancies between the interferometric and model results that deserve further investigation. We found that temperatures from line studies reported in the literature tend to underestimate the effective temperature (by about 4%) compared to values we derive from fits of the SED and our interferometric sizes. This may result from our incomplete exploration of the atmospheric parameters, differences in the line and continuum formation regions, or the presence of unknown binaries. For example, fainter companions are generally cooler, and they may contribute to making the spectrum appear as if it were due to a star that is slightly cooler than the actual temperature.

Another noteworthy discrepancy was found between the observed and SED-predicted angular diameter for the B-supergiant HD 198478 (55 Cyg). While our derived physical radius agrees with results from detailed line studies (Kraus et al. 2015), the model SED for derived size and temperature makes a poor fit of the SED. However, luminous B-supergiants have strong stellar wind outflows, and it may be necessary to employ models that include winds to match both the observed angular size and SED.

The combination of angular size from interferometry, distance from accurate parallaxes, and model fits of the SED makes it possible to place each target in the HR diagram. This provides a new method to explore stellar ages and distributions of the local massive stars and investigate star formation and evolutionary processes as never before. Continued observational effort to improve the number and accuracy of angular diameter measurements will lead to reliable surface brightness relations that can test models at new levels and can be applied to derive distance estimates of luminous objects such as extragalactic eclipsing binaries (Challouf et al. 2014).

This work is based on observations obtained with the Georgia State University Center for High Angular Resolution Astronomy Array at Mount Wilson Observatory. The CHARA Array is supported by the National Science Foundation under grant Nos. AST-1211929, AST-1411654, AST-1636624, and AST-1715788. Institutional support has been provided from the GSU College of Arts and Sciences and the GSU Office of the Vice President for Research and Economic Development. K.D. G. expresses her thanks for the financial support of a NASA Georgia Space Grant Fellowship. This research has made use of the Jean-Marie Mariotti Center JSDC catalog, the VizieR catalog access tool and SIMBAD database (CDS, Strasbourg, France), and data from the European Space Agency (ESA) mission *Gaia* (<https://www.cosmos.esa.int/gaia>), processed by the *Gaia* Data Processing and Analysis Consortium (DPAC, <https://www.cosmos.esa.int/web/gaia/dpac/consortium>). Funding for the DPAC has been provided by national institutions, in particular the institutions participating in the *Gaia* Multilateral Agreement.

Software: TLUSTY (Lanz & Hubeny 2007), ATLAS9 (Kurucz 1992; Castelli & Kurucz 2004).

ORCID iDs

Kathryn D. Gordon  <https://orcid.org/0000-0003-1338-531X>
 Douglas R. Gies  <https://orcid.org/0000-0001-8537-3583>
 Gail H. Schaefer  <https://orcid.org/0000-0001-5415-9189>
 Daniel Huber  <https://orcid.org/0000-0001-8832-4488>
 Michael Ireland  <https://orcid.org/0000-0002-6194-043X>

References

- Adelman, S. J., Caliskan, H., Gulliver, A. F., & Teker, A. 2006, *A&A*, **447**, 685
- Alekseeva, G. A., Arkharov, A. A., Galkin, V. D., et al. 1996, *BaltA*, **5**, 603
- Baines, E. K., Armstrong, J. T., Schmitt, H. R., et al. 2018, *AJ*, **155**, 30
- Balega, I. I., Balega, Y. Y., Maksimov, A. F., et al. 2007, *AstBu*, **62**, 339
- Bourgès, L., Lafrasse, S., Mella, G., et al. 2014, in ASP Conf. Ser. 485, *Astronomical Data Analysis Software and Systems XXIII*, ed. N. Manset & P. Forshay (San Francisco, CA: ASP), 223
- Boyajian, T. S., McAlister, H. A., Baines, E. K., et al. 2008, *ApJ*, **683**, 424
- Burnashev, V. I. 1985, *AbaOB*, **59**, 83
- Castelli, F., & Kurucz, R. L. 2004, arXiv:astro-ph/0405087
- Cenarro, A. J., Cardiel, N., Gorgas, J., et al. 2001, *MNRAS*, **326**, 959
- Cenarro, A. J., Peletier, R. F., Sánchez-Blázquez, P., et al. 2007, *MNRAS*, **374**, 664
- Challouf, M., Nardetto, N., Mourard, D., et al. 2014, *A&A*, **570**, A104
- Che, X., Monnier, J. D., Zhao, M., et al. 2011, *ApJ*, **732**, 68
- Chelli, A., Duvert, G., Bourgès, L., et al. 2016, *A&A*, **589**, A112
- Chesneau, O., Dessart, L., Mourard, D., et al. 2010, *A&A*, **521**, A5
- Choi, J., Dotter, A., Conroy, C., et al. 2016, *ApJ*, **823**, 102
- Claret, A., & Bloemen, S. 2011, *A&A*, **529**, A75
- Cutri, R. M., Skrutskie, M. F., van Dyk, S., et al. 2003, *yCat*, **2246**, 0
- Cutri, R. M., Wright, E. L., Conrow, T., et al. 2012, Explanatory Supplement to the WISE All-Sky Data Release Products, WISE Technical Report, **1C**
- Dotter, A. 2016, *ApJS*, **222**, 8
- Fitzpatrick, E. L., & Massa, D. 1999, *ApJ*, **525**, 1011
- Fitzpatrick, E. L., & Massa, D. 2005, *AJ*, **129**, 1642
- Fu, H.-H., Hartkopf, W. I., Mason, B. D., et al. 1997, *AJ*, **114**, 1623
- Gaia Collaboration, Brown, A. G. A., Vallenari, A., et al. 2018, *A&A*, **616**, A1
- Głębocki, R., & Gnański, P. 2005, in ESA Special Publication 560, 13th Cambridge Workshop on Cool Stars, Stellar Systems and the Sun, ed. F. Favata, G. A. J. Hussain, & B. Battrock (Noordwijk: ESA), 571
- Gordon, K. D., Gies, D. R., Schaefer, G. H., et al. 2018, *ApJ*, **869**, 37
- Gossage, S., Conroy, C., Dotter, A., et al. 2018, *ApJ*, **863**, 67
- Gullikson, K., Kraus, A., & Dodson-Robinson, S. 2016, *AJ*, **152**, 40
- Hanbury Brown, R., Davis, J., Lake, R. J. W., & Thompson, R. J. 1974, *MNRAS*, **167**, 475
- Hartkopf, W. I., Mason, B. D., McAlister, H. A., et al. 2000, *AJ*, **119**, 3084
- Henrichs, H. F., de Jong, J. A., Verdugo, E., et al. 2013, *A&A*, **555**, A46
- Hillier, D. J., & Miller, D. L. 1998, *ApJ*, **496**, 407
- Horch, E., Ninkov, Z., van Altena, W. F., et al. 1999, *AJ*, **117**, 548
- Ireland, M. J., Mérand, A., ten Brummelaar, T. A., et al. 2008, *Proc. SPIE*, **7013**, 701324
- Jamar, C., Macau-Hercot, D., Monfils, A., et al. 1976, in ESA Scientific Report 27, *Ultraviolet Bright-star Spectrophotometric Catalogue* (Noordwijk: ESA)
- Jones, J., White, R. J., Quinn, S., et al. 2016, *ApJL*, **822**, L3
- Kounkel, M., Covey, K., Suárez, G., et al. 2018, *AJ*, **156**, 84
- Kraus, M., Haucke, M., Cidale, L. S., et al. 2015, *A&A*, **581**, A75
- Kurucz, R. L. 1992, in IAU Symp. 149, *The Stellar Populations of Galaxies*, ed. B. Barbuy & A. Renzini (Dordrecht: Kluwer), 225
- Lancon, A., & Rocca-Volmerange, B. 1992, *A&AS*, **96**, 593
- Lanz, T., & Hubeny, I. 2007, *ApJS*, **169**, 83
- Le Borgne, J.-F., Bruzual, G., Pelló, R., et al. 2003, *A&A*, **402**, 433
- Lyubimkov, L. S., Rostopchin, S. I., & Lambert, D. L. 2004, *MNRAS*, **351**, 745
- Maestro, V., Che, X., Huber, D., et al. 2013, *MNRAS*, **434**, 1321
- Maestro, V., Kok, Y., Huber, D., et al. 2012, *Proc. SPIE*, **8445**, 84450G
- Maíz Apellániz, J., Alfaro, E. J., & Sota, A. 2008, arXiv:0804.2553
- Massa, D., & Fitzpatrick, E. L. 2000, *ApJS*, **126**, 517
- McAlister, H. A., ten Brummelaar, T. A., Gies, D. R., et al. 2005, *ApJ*, **628**, 439
- Morales, C., Orozco, V., Gómez, J. F., et al. 2001, *ApJ*, **552**, 278
- Morrell, N., & Levato, H. 1991, *ApJS*, **75**, 965
- Mourard, D., Clause, J. M., Marcotto, A., et al. 2009, *A&A*, **508**, 1073
- Mugnes, J.-M., & Robert, C. 2015, *MNRAS*, **454**, 28
- Neckel, T., Klare, G., & Sarcander, M. 1980, *BICDS*, **19**, 61
- Nieva, M.-F., & Przybilla, N. 2014, *A&A*, **566**, A7
- Pan, X., Shao, M., & Kulkarni, S. R. 2004, *Natur*, **427**, 326
- Pasinetti Fracassini, L. E., Pastori, L., Covino, S., & Pozzi, A. 2001, *A&A*, **367**, 521
- Paxton, B., Cantiello, M., Arras, P., et al. 2013, *ApJS*, **208**, 4
- Petrie, R. M., & Ebbighausen, E. G. 1961, *PASP*, **73**, 332
- Prugniel, P., & Soubiran, C. 2001, *A&A*, **369**, 1048
- Puls, J., Urbaneja, M. A., Venero, R., et al. 2005, *A&A*, **435**, 669
- Santolaya-Rey, A. E., Puls, J., & Herrero, A. 1997, *A&A*, **323**, 488
- Savage, B. D., Massa, D., Meade, M., & Wesselius, P. R. 1985, *ApJS*, **59**, 397
- Schaefer, G. H., Hummel, C. A., Gies, D. R., et al. 2016, *AJ*, **152**, 213
- Soubiran, C., Le Campion, J.-F., Brouillet, N., & Chemin, L. 2016, *A&A*, **591**, A118
- Swihart, S. J., Garcia, E. V., Stassun, K. G., et al. 2017, *AJ*, **153**, 16
- ten Brummelaar, T., Mason, B. D., McAlister, H. A., et al. 2000, *AJ*, **119**, 2403
- ten Brummelaar, T. A., McAlister, H. A., Ridgway, S. T., et al. 2005, *ApJ*, **628**, 453
- ten Brummelaar, T. A., Sturmann, J., Ridgway, S. T., et al. 2013, *JAI*, **2**, 1340004
- Underhill, A. B., Divan, L., Prevot-Burnichon, M.-L., & Doazan, V. 1979, *MNRAS*, **189**, 601
- Valdes, F., Gupta, R., Rose, J. A., Singh, H. P., & Bell, D. J. 2004, *ApJS*, **152**, 251
- van Leeuwen, F. 2007, *A&A*, **474**, 653
- Wheelwright, H. E., Oudmaijer, R. D., & Schnerr, R. S. 2009, *A&A*, **497**, 487
- White, T. R., Pope, B. J. S., Antoci, V., et al. 2017, *MNRAS*, **471**, 2882
- Wu, Z.-Y., Zhou, X., Ma, J., & Du, C.-H. 2009, *MNRAS*, **399**, 2146
- Zorec, J., Cidale, L., Arias, M. L., et al. 2009, *A&A*, **501**, 297
- Zwahlen, N., North, P., Debernardi, Y., et al. 2004, *A&A*, **425**, L45